JJEES
Jordan Journal of Earth and Environmental Sciences

Volume 6, Number 1, September, 2014
ISSN 1995-6681
Pages 37- 43

SRAD Radial Diagram: A New Way to Display Important Aspects of Fault-Slip Analysis Results

Alireza Yousefi Bavil*

Department of Geotectonics and Regional Geology, Geology Institute of Azerbaijan, Baku, Azerbaijan

Received 12 April, 2013; Accepted 7 September, 2014

Abstract

Aspects of stress inversion, such as angular deviation, stress ratio, orientation of the principal stress axes, and the normal and shear components of the resolved stress tensor on a fault plane, are given as output by many programs that address stress inversion. However, comparison of results becomes difficult when the number of stress states and associated parameters increases. A stress ratio–angular deviation radial diagram was constructed. The diagram provides simultaneous illustration of the above parameters and facilitates the comparison and interpretation of up to eleven various stress states. The application of the diagram is demonstrated by a worked example based on data obtained from the Tabriz North Fault in the Eastern Azerbaijan province NW of Iran.

Keywords: Angular deviation; Radial diagram; Stress ratio; Stress tensor, Tabriz North Fault

1. Introduction

Since the 1970s, various methods have been introduced to determine (paleo) stress conditions from homogeneous and heterogeneous fault-slip data (e.g. Carey and Brunier, 1974; Angelier, 1979, 1984; Etchecopar et al.,1981; Armijo et al.,1982; Simón-Gómez, 1986; Lisl,e 1987, 1988; Galindo-Zaldívar and González-Lodeiro, 1988; Huang, 1988; Hardcastle and Hills, 1991; Nemcok and Lisle, 1995; Fry 1999; Yamaji, 2000; Delvaux and Sperner, 2003). Recently, new methods have been introduced to analyze heterogeneous fault-slip data based on cluster analysis (Nemcok and Lisle, 1995), Fry's graphical procedure, 1999, or the multiple inverse method (Yamaji, 2000). Angelier,1994, Liesa and Lisle, 2004, and Célérier, et al., 2012. have scrutinized and reviewed most of the above-mentioned methods.

Stress inversion techniques treat faults and their slip vectors as paleostress gauges recording the direction of maximum resolved shear stress on the planes of the faults. The directional characteristics of shear stress on planes of different attitude are sufficient to constrain certain features of the geological stress condition, namely the orientations of the principal stress axes (σ_1, σ_2, σ_3) and stress ratio (Φ or R) (e.g. Wallace, 1951; Bott, 1959; Bishop, 1966; Angelier, 1979, 1984; Lisle and Orife, 2002; Delvaux and Sperner, 2003).

The majority of computer programs that deal with stress inversion techniques utilize some criteria of best fit. In this manner, such programs consider the lowest mean deviation or lowest mean-square deviation between the observed slickenlines and the direction of maximum shear stress predicted from the stress tensor, which is known as the deviation angle δ (hereafter, the first criterion). A mechanical criterion is typically used to check the reactivation compatibility of faults via restraining fault orientation to high shear stress τ and lower compressive normal stress σ_n (hereafter, the second criterion) (Célérier, 1988; Angelier, 1990; Ramsay and Lisle, 2000). A detailed review of these criteria has been presented by Célérier, et al., 2012.

Usually, depending on the heterogeneity of the data set, more than one set of stress conditions can result from a stress inversion analysis; these condition sets will typically exhibit some differences with respect to a given parameter or criterion. The opportunity for simultaneous consideration of the results of both the geometrical and mechanical criteria applied, as well as the other parameters resulting from stress inversion, can facilitate the study of various stress tensors. This permits better assessment of the suitability of a certain stress state for the reactivation of a set of fault-slip data and for the comparison of different stress inversion parameters. Here, a diagram is introduced that serves as a histogram and allows the study of the results of up to eleven various stress states simultaneously. Furthermore, it permits comparison of two criteria for individual stress states and allows comparison of all defined stress states with respect to these criteria and some other parameters that can be attributed to stress state.

* Corresponding author. e-mail: ayousefi@gia.ab.az

2. Diagram's constituent parameters

2.1. Angular deviation

Angular deviation, which results from different methods of stress inversion, is usually the principal parameter used for assessing the relation between a given stress state and a set of fault-slip data (Carey and Brunier, 1974; Angelier, 1979; Lisle, 1987; Ramsay and Lisle, 2000; Yamaji, 2000; Célérier et al.,2012). Depending on the precision desired, different angles (e.g. 10°, 20°, and 30°) are used as critical values to restrain the relation between fault-slip data and a driven stress state. Various methods can be used to represent δ, including stereograms, tables, Venn diagrams, and histograms. However, the first three methods can cause perplexity during the classification of δ and the determined stress tensors. In most programs applying inversion methods, histograms are usually used to represent the frequency of fault-slip data satisfying different criteria of δ. This type of histogram, together with an associated Mohr diagram, provides information about δ directly and Φ indirectly.

2.2. Stress ratio

A Mohr diagram shows the predicted levels of τ and σ_n, i.e., the Mohr point, for all the measured faults in relation to a sliding envelop and presents a visual appreciation of the suitability of a given tensor for explaining the observed slip on the faults. In the context of brittle failure and faulting, τ and σ_n are two resolved components of the stress vector on a given plane, which is a result of internal forces acting on imaginary surfaces of a body (Ramsay and Lisle, 2000). On a specified plane, the shear stress component τ is effective parallel to the plane, whereas the normal stress component σ_n is effective perpendicular to the plane. Their combination is one of the parameters controlling the characteristics of slip on a fault surface. As principal stress values are not obtained through stress inversion, the ratio of the differences between the principal stress values are determined relatively, which defines Φ (Bott, 1959; Célérier, 1995; Lisle and Orife, 2002). For example, according to Bishop (1966) and Angelier (1975), the value of stress ratio is determined by:

$$\Phi = (\sigma_2 - \sigma_3) / (\sigma_1 - \sigma_3) \quad (1)$$

where $\sigma_1 \geq \sigma_2 \geq \sigma_3$ and where the positive sign refers to compression. By definition, the value of Φ ranges between 0 and 1, represented by $\sigma_1 \geq \sigma_2 \geq \sigma_3$ and $\sigma_1 = \sigma_2 > \sigma_3$, respectively. The adoption of the above stress ratio is mentioned here because the inversion method in Yamaji's multiple inverse method (MIM) program is based on Bishop's version of stress ratio (Yamaji et al.,2010). However, there are different adoptions available, e.g. Nádai's μ (Nádai, 1931 p. 77), Carey's R (Carey and Mercier, 1987), and Lisle's R (Lisle, 1989). Their formulations are provided in Appendix A.

3. Diagram inputs and adopted criteria

Stress ratio and δ are the principal parameters upon which the diagram is established. The Mohr point parameters related to each defined stress state and the orientation of principal stress axes, e.g.$\overrightarrow{\sigma_1}$. , are also used in the diagram. Most of the above-mentioned parameters are usually provided as program output, e.g. for Yamaji's MIM program (Yamaji, 2000). The stress inversion results for analysis are placed in an Excel file, in which each row corresponds to the data of one fault slip; however, the first row is allocated to $\overrightarrow{\sigma_1}$. Considering the range of Φ (i.e., 0–1 with intervals of 0.1), 11 and 22 columns are required for δ and (σn, τ), respectively. In this work, values for δ, σ_n, τ, and $\overrightarrow{\sigma_i}$ are allocated for each fault-slip datum and each recognized stress state, respectively.

Three critical values of δ (i.e., 10°, 20°, and 30°) are chosen as the first criterion. Meanwhile, the Mohr point of the faults that satisf $\tau \geq \mu\sigma_n$ is adopted as the second criterion, where μ is the coefficient of residual friction for sliding on a pre-existing fault (Žalohar and Vrabec, 2007). The fault-slip data used in the example are collected from sandstones; thus, the value of μ is set at 0.51 (Schellart, 2000).

4. Establishment of stress ratio–angular deviation (SRAD) diagram

Code is written in MatlabTM to construct the SRAD radius diagram. The radial form is chosen both for easier visualization and for comparison of the statistics resulting from the stress inversion. Consequently, a circle formulation is used in the writing of the code. In an x–y Cartesian coordinate system, the circle with center coordinates (a, b) and radius r is a set of all points (x, y) in which:

$$(x-a)^2 + (y-b)^2 = r^2 \quad (2)$$

Any point (x, y) on the circle has length x–a and y–b. If the circle is centered at the origin (0, 0), then the equation can be written as:

$$x = r\cos t \quad (3)$$

and

$$y = r\sin t \quad (4)$$

where r is the angular deviation and t is the angle that the radius—with a given value of Φ—from (a, b) to (x, y) makes with the x-axis in the range of 0–90°, where 0° and 90° refer to Φ = 0 and 1, respectively.

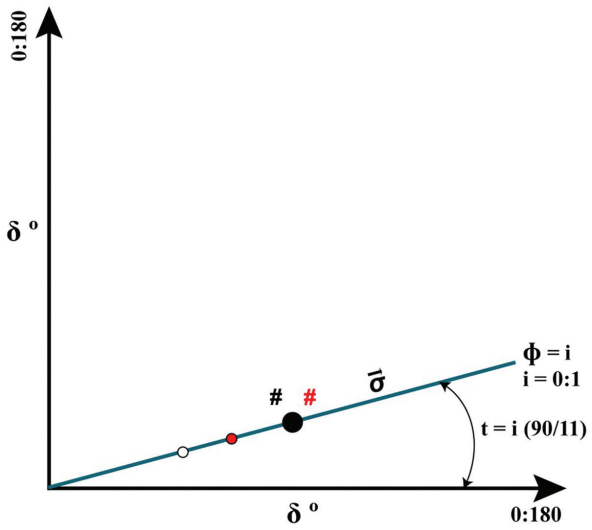

Figure 1: Components and basics of the SRAD diagram established based on the parameters of stress ratio Φ and angular deviation δ. A given stress state with a certain Φ value (i.e. i = 0 to 1, where i represents the Φ interval number) is represented by a ray that makes a given angle (t) with respect to the horizontal axis, calculated ast=i. (90/11). The ray length ranges between 0° and 180°, where the position of small circles (both white and red) denotes the δ value of each fault within the data set with respect to the defined stress state. White and red circles denote faults satisfying only the geometrical and both the geometrical and mechanical criteria, respectively. The black circle shows the position of a critical value of δ. Black and red # symbols denote the frequencies of faults, at a given critical value, that satisfy the first criterion and both criteria, respectively. Along a ray (i.e. a defined stress state), $\overrightarrow{\sigma}$ denotes the orientation of the principal stress axis that corresponds to the stress state.

The SRAD radial diagram consists of 11 radii. These radii are allocated to 11 intervals of Φ and each radius includes the values of δ for all fault-slip data with respect to a given defined stress state with a certain value of Φ (Fig. 1). Using three critical deviation angles, the values of δ are bounded as 0–10°, 0–20°, and 0–30° and the sum of the faults that meet the criteria are calculated for each bin. Also, of defined stress states with given Φ values are allocated to the same Φ radii (i.e., Φ interval) on the diagram.

The radial form of Φ intervals in the diagram evokes the diagram for representing stress tensors introduced by Ramsay and Lisle (2000); however, these diagrams are based on different concepts. Ramsay and Lisle's diagram is based on the parameters σ_1, σ_2, and σ_3 and displays the location (i.e., stress shape ratio and the differential stresses) of a stress tensor between Φ = 0 and Φ = 1. However, the diagram in this study is based on σ_n, τ, δ, and Φ and displays the attributes of correlation between a given stress state, a set of faults, and associated slip directions. In other words, in Ramsay and Lisle's diagram, Φ is output data, whereas in the diagram in this study, Φ is input data for the diagram.

5. Applications

During the comparison of different stress conditions (which can be determined under similar or different tectonic regimes and by different sources, i.e., geologic or seismic), in addition to the geometrical and mechanical criteria, it is sometimes important to consider those statistical criteria either adopted before applying the inversion or derived from it. Other stress field parameters can be involved in the comparison; however, these are approached in different ways, e.g. tectonic regime (γ) (Célérier, 1995). Unlike ordinary histograms, the SRAD radial diagram provides an opportunity to illustrate different parameters with different characteristics (e.g. orientation, frequency, eigenvector, and eigenvalue) and different value ranges (e.g. frequency, octahedral shear stress, and standard deviation).

The diagram allows the study and comparison of up to eleven stress tensors simultaneously and the simultaneous comparison of the geometrical and mechanical criteria for an individual state. Furthermore, the comparison can be expanded depending on the parameters allocated to the stress state, i.e., the tectonic regime parameter (γ) (Célérier, 1995), principal stress axes, differences between each tensor and the mean stress tensor, eigenvectors and eigenvalues of the stress state, octahedral shear stress (τ_{oct}) (Lisle and Orife, 2002; Orife and Lisle, 2003), and differences between angular stress distance (Θ), and mean angular stress difference (Θ^-). Moreover, regarding the MIM program, the diagram also allows the study of the enhance factor (EF), dispersion factor (DF), fault combination number (K), number of tensors plotted on each stereogram (N_p), number of different stress states output by the program (N_s), and standard deviation (SD) (Yamaji, 2000; Yamaji et al.,2010).

Depending on the parameters transferred to the diagram, it allows the display of two patterns of variation across different values of Φ (due to the 'across-ray' differences between various stress states) and δ (due to 'along-ray' changes in fault angular deviations with respect to an individual stress state).

6. A worked example

In this example, the parameters transferred to the diagram are δ, σ_n, τ, and $\overrightarrow{\sigma_1}$. The illustration of the across-ray differences allows the simultaneous comparison of the frequency of faults satisfying the following: (1) the first criterion, (2) both the first and second criteria, and (3) $\overrightarrow{\sigma_1}$. The illustration of along-ray changes allows the comparison of the frequency of faults satisfying the first criterion (δ) and both criteria (δ, σ_n, and τ) for a given critical value. This last illustration (i.e. along-ray changes) provides a similar function to an ordinary histogram.

The MIM program main processor (version 6) was used to apply a stress inversion on a real data set. The program allows the separation of deviatoric stresses using cluster analysis without a priori information on the stresses (Menke, 1989), which utilizes a form of self-correlation of data (Yamaji, 2000).

6.1. Geological setting

Fault-slip data (i.e., the attitude of faults and associated slickenlines) were collected from an area around the NW segment of the Tabriz North Fault (TNF), which is an area on the Ayanli Mountain between the Aji-chay and Arpa-dere rivers (Fig. 2). The study area is covered both by the youngest lithological units of the Miocene, i.e., red sandstone with marl, and by Quaternary sediments. The layers are almost horizontal (dip angle is about 6°). The deformation and uplift of these lithological units are ascribed to epeirogenic activity during the Pliocene–Quaternary Pasadenian structural stage (Geological Survey of Iran, 1993). Right-lateral displacement along this strand of the TNF is conspicuous by the deflection of drainage channels on the Quaternary sediments (Karakhanian et al.,2004). Within the study area, faults with both NW–SE and NE–SW trends cross cut and displace each other; however, the cross cutting of the NE–SW-trending faults by the NW–SE-trending faults are more frequent. Slickenlines' superposition is not found in the sampled faults (37 fault-slip data). The tectonic setting mentioned above suggests low heterogeneity of the data set.

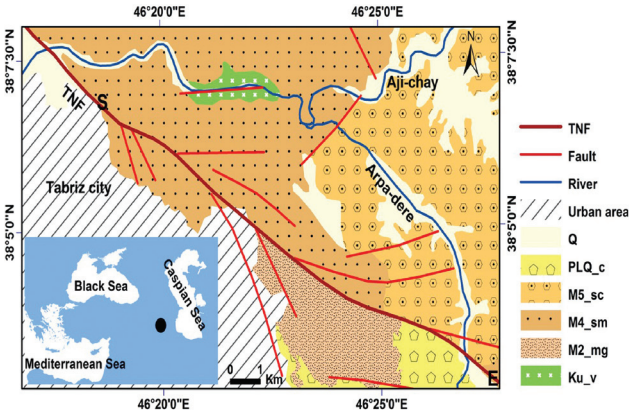

Figure 2: Geologic map around the NW segment of the TNF, showing red conglomerates with sandstone (M_5^{sc}), red sandstone with marl (M_4^{sm}), gypsiferous marl (M_2^{mg}), and basic and ultrabasic rocks (K_u^v). The black solid circle in the inset denotes the location of the study area. S and E define the start and end points of the swath profile. Tabriz city is located on the SW slope of the Aynali Mountain, which is located mainly to the NE of the TNF

6.2. Inversion procedure and results

At the first attempt at inversion, seven fault-slip data were found incompatible with any of the defined stress states and their separate inversion did not reveal a stable stress tensor. Therefore, these data were considered spurious and were excluded from the data set. The results of the secondary inversion, on the remaining 30 fault-slip data (Fig. 3a), did not change dramatically; therefore, the defined stress tensors are oriented almost coaxially.

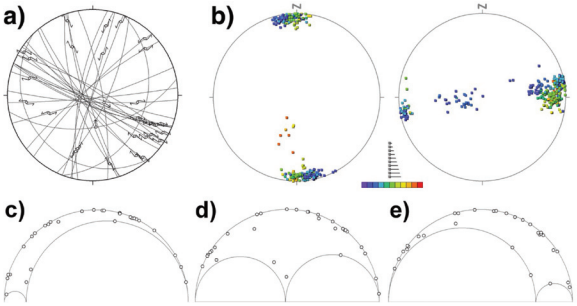

Figure 3: (a) Stereographic projection of fault-slip data and (b) recognized stress tensors. Fault-slip data were collected around the NW segment of the TNF. Stress tensors have been recognized by applying the multiple inverse method (program MIM) to the fault-slip data. In part (b), each square delineates the attitude of σ_1 (in the left stereogram) and σ_3 (in the right stereogram). Tensor colors show the Φ value: violet (Φ = 0), red (Φ = 1). Mohr points (τ and σ_n) of collected fault-slip data are illustrated with respect to three determined stress states: (c) Φ = 0.12, (d), Φ = 0.49, and (e) Φ = 0.8.

To treat the stress tensors (each square in the stereogram) recognized by MIM (Fig. 3b) objectively, to be precise about the location of the defined stress state(s), and to study the differences and their significance, the parameters of all defined states were calculated by the program, without any human intervention at this stage. Therefore, those stress states including all values of Φ, regardless of whether they formed a cluster, were taken into account. The inversion yields nine stress states with differing cluster densities, which include all tensors with different Φ values, i.e., 0.1–0.9 (Fig. 4).

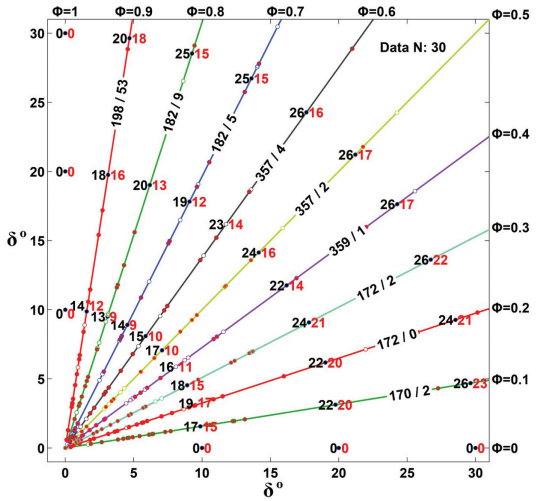

Figure 4: SRAD diagram illustrating the results of stress inversion on 30 fault-slip data collected along the NW segment of the TNF (modified after Yousefi Bavil and Moayyed, in press, 2015). Each ray is related to the defined stress state with a certain Φ value and involves the deviation angle δ of all fault-slip data (faults with values of δ greater than about 30–35° cannot be seen in the diagram) with respect to that state, whereas each circle on each radius indicates a fault's δ. The basics and parameters of the diagram have been described in Fig. 1.

Note that, in this study, three terms are used in the different stages of inversion analysis. (1) 'Recognized stress tensor' refers to a given tensor calculated by the MIM program (Fig. 3b, each square in the stereogram). (2) 'Defined stress state' refers to a given state composed of different stress tensors with the same Φ interval value, chosen objectively with no human interference based on their Φ values (Fig. 4). (3) 'Determined stress state' refers to a given stress state composed of one or more defined stress states—similar stress states, but with different Φ values. The last identified state is based on human decision. In this context, the SRAD diagram helps extend the objective stage of the decision-making procedure during the investigation of defined states with respect to various parameters.

6.3. Observations from the SRAD diagram

Surveying the diagram and the across-ray variation pattern obtained in this example (Fig. 4) demonstrates the following:

(1) For all critical values (δ = 10°, 20°, and 30°), the frequency of those faults that satisfy only the first criterion (black frequency numbers) is greater than that of those that satisfy both criteria (red frequency numbers). According to the first criterion, each of the defined stress states with Φ = 0.1 to 0.8 causes instability in more than 80% of faults where δ = 30°.

(2) The frequency of faults that satisfy both criteria generally decreases as Φ increases. This frequency is greater for states with Φ = 0.1 to 0.3 comparing other stress states. The value, i.e., frequency, reaches more than 70% of all faults with respect to the stress states with Φ = 0.1 to 0.3. Furthermore, even though some fault-slip data do not meet the first criterion exactly, i.e., δ > 30°, they are suitable for reactivation with regard to both criteria, where δ is slightly more than 30° (i.e., in cases with Φ = 0.2, 0.5, 0.7, and 0.8).

(3) A stress state with Φ = 0.9 has a different $\overrightarrow{\sigma_1}$ compared with other stress states.

(4) Among the stress states with Φ = 0.1 to 0.8, the value of Δ (which results from the difference between the frequency of faults satisfying the first criterion and both criteria at a given critical δ value) is lower for stress states with Φ = 0.1 to 0.3 than for stress states with other Φ values.

6.4. Stress state differences

The STRESSTAT program (Lisle and Orife, 2002) was used to compare the differences of the defined stress states. According to Orife and Lisle (2003), the difference between two normalized tensors can be expressed by a single parameter, the 'tensor difference' D. They introduced four terms with an accompanying range of values: Very similar, D < 0.66; Similar, D = 0.66 to 1.01; Different, D = 1.01 to 1.71; and Very different, D > 1.71. These terms can be used for the qualitative description of stress difference between any two stress tensors.

The differences between nine defined states show that the maximum value of D (D_{max}) among all defined stress states is equal to 1.0189, which corresponds to the difference between states with Φ = 0.1 and 0.9 (Table 1, number 4). Among eight stress states (Φ = 0.1 to 0.8) with similar principal stress axes, D_{max} is equal to 0.8696, which indicates their similarity (Table 1, number 1). Furthermore, among three stress states with proximity in terms of Φ (i.e., 0.1 to 0.3) and frequency number, D_{max} is equal to 0.2508, suggesting that the tensors are very similar (Table 1, number 2).

Table 1: Parameters of seven determined stress states in different Φ ranges. σ_1, σ_2, and σ_3 are orientations of three principal stress axes (where $\sigma_1 \geq \sigma_2 \geq \sigma_3$); Φ denotes the stress ratio according to Bishop's adoption; D_{max} and Nrt indicate the maximum stress tensor difference and number of recognized tensors in the stereogram for the constituent states of determined stress states, respectively.

Determined stress state		Parameters of mean stress tensor					
Number	Φ range	σ_1	σ_2	σ_3	Φ	D_{max}	N_{rt}
1	0.1–0.8	174.5 / 0.1	264.9 / 77.8	84.4 / 12.2	0.32	0.8696	270
2	0.1–0.3	170.9 / 1.3	273.4 / 84.1	80.8 / 05.8	0.12	0.2508	147
3	0.9	198.4 / 52.7	344.7 / 32.4	85.6 / 16.5	0.91	-	5
4	0.1–0.91	174.5 / 0.2	265.4 / 77.5	84.5 / 12.5	0.33	1.0189	275
5	0.0–0.330	170.9 / 1.3	273.4 / 84.1	80.8 / 05.8	0.12	0.2508	147
6	0.331–0.660	357.7 / 2.0	259.7 / 75.8	88.2 / 14.1	0.49	0.2656	99
7	0.661–1.0	182.0 / 8.8	303.9 / 73.8	89.9 / 13.6	0.80	0.3669	29

6.5. Interpretation

According to Orife and Lisle (2003), the absolute value of the stress ratio is a first approximation to the tensor difference measure (D), where the principal axes of stress tensors are coaxial. This is the case for the constituent states of the first determined stress state (Table 1, number 1), where the defined states with Φ = 0.1 to 0.8 are approximately coaxial and only their values of Φ are different. However, considering that, among the states, D_{max} = 0.8696, and according to the ranges introduced by Orife and Lisle (2003), the Φ difference of the states is insufficient to classify them as different stress states. The inclusion of states with Φ = 0.1 to 0.2 within the first determined state is preferred (rather than the inclusion of the state with Φ = 0.9) because, except for the last state, the others are coaxial and refer to the same tectonic setting (i.e., strike-slip). Therefore, two significant stress states are determined with respect to the stress difference measure D (Table 1, numbers 1, 2).

The average parameters of the two determined states refer to the strike-slip tectonic setting; however, the defined states of the second determined state are the most significant regarding the satisfaction of both criteria (Fig. 4) and the cluster density of the recognized stress tensors (Fig. 3; Table 1). In addition, the frequency of faults satisfying both criteria decreases as Φ increases (Fig. 4). This deduction, which has been facilitated by the diagram, allows the more accurate restraining of the average stress tensor during its determination. Furthermore, the similar lithological units without superposition of slickenlines on collected fault surfaces, indicating a single structural phase, in conjunction with the similarity of the stress states, demonstrate that the determined states belong to the modern stress phase.

The strike-slip tectonic setting and the trend of $\overrightarrow{\sigma_1}$ are also consistent with: (1) the results of the fault plane solutions of Talebian and Jackson (2002) and Moradi et al. (2011), showing an approximate NNW–SSE-trending compressive stress; (2) the N–S shortening trend and the right-lateral displacements deduced from GPS measurements by Vernant et al.,(2004).

The classification of defined stress states with respect to their stress ratios and cluster densities (Table 1, numbers 5–7) also reveals that the fault displacements are mainly a result of compressional rather than extensional stress regimes, i.e., only about 11% of the recognized tensors are extensional (Fig. 3c–e). This deduction is supported by geomorphic and tectonic geomorphology evidence. In this regard, the elevated area on the NE side of the TNF, in comparison with the lower area on the SW side of the fault (Fig. 2 and 5), indicates an intensified uplift history on the NE side. In this respect, measurement of elevation changes along a swath profile (Fig. 5) reveals the average elevation range (i.e., maximum elevation - minimum elevation) to be 266 m. Furthermore, according to Yousefi Bavil (2012), the responses of streams flowing on the Aynali Mountain, in respect to the relative vertical displacements along their longitudinal profiles, reveal unstable and nearly linear or convex longitudinal profiles that indicate ongoing uplift and young orogenic activity.

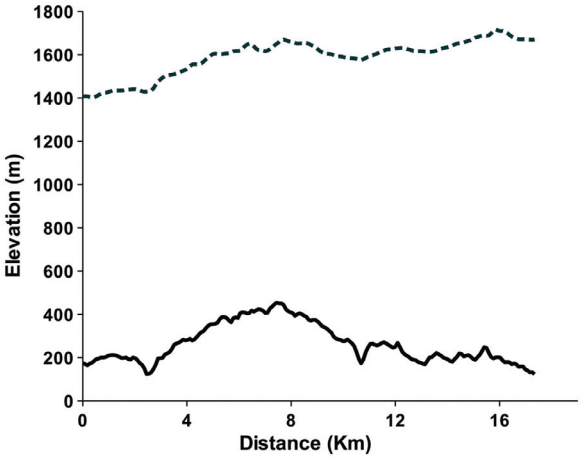

Figure 5: Elevation changes between the NE and SW sides of the TNF along a swath profile with length and width of approximately 17 and 5.3 km, respectively. The start and end points of the swath profile (i.e., S and E) are shown in Fig. 2. The solid line represents the elevation range (maximum elevation - minimum elevation) and the dashed line denotes mean elevation. The average value of the elevation range is 266 m.

The above-mentioned evidence (i.e., lithologic, kinematic, tectonic geomorphology, seismic, and remote sensing evidence) combined with the statistical results (i.e., very low-stress tensor cluster density) does not support the presumption that extensional stress states with $\Phi > 0.66$ (Table 1, number 7) are significant stress states responsible for the brittle deformation within the study area.

7. Conclusions

The SRAD diagram established on the parameters of stress ratio and angular deviation allows the following:

(1) the simultaneous illustration of the different parameters resulting from a stress inversion analysis;

(2) a reduction in classification perplexity of δ caused by conventional clustering methods, e.g. stereograms and Venn diagrams;

(3) an increase in the number of parameters available for mutual comparison (it also facilitates the illustration and, therefore, the comparison of parameters with different characteristics and value ranges); and

(4) the comparison and interpretation of up to eleven various stress states, including the entire range of Φ.

Acknowledgements

Thanks go to the two anonymous reviewers whose comments and suggestions were helpful in improving the manuscript. The author is grateful to Bernard Célérier for his suggestion on the mechanical criterion that helped to improve the quality of the criterion.

Appendix A

In addition to Bishop's Φ, which is the most common version of stress ratio, there are other adoptions of stress ratio formulated by different authors, including the following. Nadai's $\mu = (2\sigma_2 - \sigma_1 - \sigma_3)/(\sigma_1 - \sigma_2)$ (Nádai 1931 p. 77)

Carey's $R = (\sigma_1 - \sigma_2)/(\sigma_1 - \sigma_3)$ (Carey and Mercier 1987)

Lisle's $R = (\sigma_2 - \sigma_3)/(\sigma_1 - \sigma_2)$ (Lisle 1989)

References

[1] Angelier, J., 1975. Sur l'analyse de mesures recueillies sans des sites faillés: l'utilité d'une confrontation entre les méthodes dynamiques et cinématiques. Comptes Rendus de l'Académe des Sciences, Paris D281, 1805–1808.

[2] Angelier, J., 1979. Determination of the mean principal directions of stresses for a given fault population, Tectonophysics, 56(3–4):T17–T26.

[3] Angelier, J., 1984. Tectonic analysis of fault slip data sets, Journal of Geophysical Research, 89:5835–5848.

[4] Angelier, J., 1990. Inversion of field data in fault tectonics to obtain the regional stress—III. A new rapid direct inversion method by analytical means, Geophysical Journal International, 103: 363–376.

[5] Angelier, J., 1994. Fault slip analysis and palaeostress reconstruction. In: Hancock, P.L., (Ed.), Continental Deformation, Pergamon, New York, pp. 53–101.

[6] Armijo, R., Carey, E., and Cisternas, A., 1982. The inverse problem in microtectonics and the separation of tectonic phases, Tectonophysics, 82:145–160.

[7] Bishop, A.W., 1966. The strength of soils as engineering materials, Géotechnique, 16:91–128

[8] Bott, M.H.P., 1959. The mechanisms of oblique slip faulting, Geological Magazine, 96:109–117.

[9] Célérier, B., 1988. How much does slip on a reactivated fault plane constrain the stress tensor? Tectonics, 7(6):1257–1278.

[10] Célérier, B., 1995. Tectonic regime and slip orientation of reactivated faults, Geophys. J. Int., 121:143-161.

[11] Célérier, B., Etchecopar, A., Bergerat, F., Vergely, P., Arthaud, F., and Laurent, P., 2012. Inferring stress from faulting: From early concepts to inverse methods, Tectonophysics, 581:206–219.

[12] Carey, E., and Brunier, B., 1974. Analyse théorique et numérique d'un modèle mécanique élémentaire appliqué à l'étude d'une population de failles, Comptes Rendus Hebdomadaires des Seances de l'Academie des Sciences, D279:891–894.

[13] Carey, E., and Mercier, J.L., 1987. A numerical method of determining the state of stress using focal mechanisms of earthquake populations: applications to Tibetan teleseismicity and microseismicity of S. Peru. Earth and Planetary Science Letters 82, 165–179.

[14] Delvaux, D., and Sperner, B., 2003. New aspects of tectonic stress inversion with reference to the TENSOR program. In: New Insights into Structural Interpretation and Modelling, edited by D.A. Nieuwland, Geol. Soc. Spec. Publ., 212, 75-100.

[15] Etchecopar, A., Vasseur, G., and Daignieres, M., 1981. An inverse problem in microtectonics for the determination of stress tensors from fault striation analysis, Journal of Structural Geology, 3:51–65.

[16] Fry, N., 1999. Striated faults: visual appreciation of their constraint on possible palaeostress tensors, Journal of Structural Geology, 21:7–21.

[17] Geological Survey of Iran, Tehran, 1993, Eastern Azerbaijan, Tabriz, 1:100000 geological series, sheet 5266, Geological Survey of Iran, Tehran.

[18] Galindo-Zaldívar, J., and González-Lodeiro, F., 1988. Faulting phase differentiation by means of computer search on a grid pattern, Annales Tectonicae, 2:90–97.

[19] Hardcastle, K.C., and Hills, L.S., 1991. Brute3 and Select—QuickBasic 4 programs for determination of stress tensor configurations and separation of heterogeneous populations of fault-slip data, Computers and Geosciences, 17:23–43.

[20] Huang, Q., 1988. Computer-based method to separate heterogeneous sets of fault-slip data into sub-sets, Journal of Structural Geology, 10:297–299.

[21] Karakhanian, A.S., Trifonov, V.G., Philip, H., Avagyan, A., Hessami, K., Jamali, F., Bayraktutan, M.S., Bagdassarian, H., Arakelian, S., Davtian, V., and Adilkhanyan, A., 2004. Active faulting and natural hazards in Armenia, eastern Turkey and northwestern Iran, Tectonophysics, 380:189–219.

[22] Liesa, C.L., and Lisle, R.J., 2004. Reliability of methods to separate stress tensors from heterogeneous fault-slip data, Journal of Structural Geology, 26(3): 559–572.

[23] Lisle, R.J., 1987. Principal stress orientations from faults: an additional constraint, Annales Tectonicae, 1:155–158.

[24] Lisle, R.J., 1988. Romsa: a Basic program for palaeostress analysis using fault-striation data, Computers and Geosciences, 14:255–259.

[25] Lisle, R.J., 1989. The statistical analysis of orthogonal orientation data. Journal of Geology 97, 360–364.

[26] Lisle, R.J., and Orife, T., 2002. STRESSTAT: a Basic program for numerical evaluation of multiple stress inversion results, Computers and Geosciences, 28:1037–1040.

[27] Menke, W., 1989. Geophysical data analysis: discrete inverse theory. Academic Press, San Diego 289.

[28] Moradi A.S., Denis Hatzfeld, D., and Tatar M., 2011. Microseismicity and seismotectonics of the North Tabriz fault (Iran), Tectonophysics, 506:22–30.

[29] Nádai, A., 1931. Plasticity. McGraw-Hill, New York, 367pp.

[30] Nemcok, M. and Lisle, R.J., 1995. A stress inversion procedure for polyphase fault/slip data sets, Journal of Structural Geology, 17:1445–1453.

[31] Orife, T., and Lisle, R.J., 2003. Numerical processing of palaeostress results, Journal of Structural Geology, 25:949–957.

[32] Ramsay, J.G. and Lisle, R.J., 2000. The Techniques of Modern Structural Geology, Vol.3, Applications of Continuum Mechanics in Structural Geology. Academic Press, London 1061pp.

[33] Schellart, W.P., 2000. Shear test results for cohesion and friction coefficients for different granular materials:

scaling implications for their usage in analogue modelling, Tectonophysics, 324:1–16.

[34] Simón-Gómez, J.L., 1986. Analysis of a gradual change in stress regime (example from the eastern Iberian Chain, Spain), Tectonophysics, 124:37–53.

[35] Talebian, M., and Jackson, J.A., 2002. Offset on the Main Recent Fault of the NW Iran and implications for the late Cenozoic tectonics of the Arabia-Eurasia collision zone, Geophys. J. Int., 150:422–439.

[36] Vernant, P., Nilforushan, F., Hatzfeld, D., Abbasi, M.R., Vigny, C., Masson, F., Nankhali, H., Martinold, J. Ashtiani, A. Tavakoli, F. and Chery, J. 2004. Present-day crustal deformation and plate kinematics in the Middle East constrained by GPS measurements in Iran and northern Oman, Geophys. J. Int., 157:38–398.

[37] Wallace, R.E., 1951. Geometry of shearing stress and relation to faulting. Journal of Geology, 59:118–130.

[38] Yamaji, A., 2000. The multiple inverse method: a new technique to separate stresses from heterogeneous fault-slip data, Journal of Structural Geology, 22:441–452.

[39] Yamaji, A., Sato, K., and Otsubo, M., 2010. Multiple inverse method software package (user's guide). <http://www.kueps.kyoto-u.ac.jp/~web-bs/tsg/software/mim> Accessed 21 March 2013.

[40] Yousefi Bavil, A., 2012. Longitudinal Profiles of Bedrock Rivers around North Tabriz and North Misho Faults: Implications for Geomorphic Fault Segmentation (Eastern Azerbaijan Province, Iran); ASM Sci. J., 6(2): 107–121.

[41] Yousefi Bavil, A., and Moayyed M. Paleo and modern stress regimes of central North Tabriz Fault (Eastern Azarbaijan province, NW Iran), Journal of Earth Science, China, (in press: vol 25, no 3, 2015).

[42] Žalohar, J., and Vrabec, M., 2007. Paleostress analysis of heterogeneous fault-slip data: The Gauss method, Journal of Structural Geology, 29:1798–1810.